

## Article

# Enhanced Solar Light-Driven Photocatalytic Degradation of Tetracycline Using Fe<sup>3+</sup>-Doped CdO/ZnS Nanocomposite: Mechanistic Insights and Performance Evaluation

R. Joyce Stella <sup>1,†</sup>, I. Sreevani <sup>1</sup>, Thirumala Rao Gurugubelli <sup>2,†</sup> , R. V. S. S. N. Ravikumar <sup>3,\*</sup>  and Ravindranadh Koutavarapu <sup>4,\*</sup> 

<sup>1</sup> Department of Humanities and Science, KSRM College of Engineering, Kadapa 516003, Andhra Pradesh, India; joycestella10@gmail.com (R.J.S.); sreevani.kadapa@gmail.com (I.S.)

<sup>2</sup> Department of Physics, School of Sciences, SR University, Warangal 506371, Telangana, India; thirumalaphy@gmail.com or g.thirumalarao@sru.edu.in

<sup>3</sup> Department of Physics, Acharya Nagarjuna University, Guntur 522 510, Andhra Pradesh, India

<sup>4</sup> Department of Robotics Engineering, College of Mechanical and IT Engineering, Yeungnam University, Gyeongsan 38541, Republic of Korea

\* Correspondence: rvssn@yahoo.co.in (R.V.S.S.N.R.); ravindra\_physicist@ynu.ac.kr (R.K.)

† These authors contributed equally to this work.

**Abstract:** In recent years, studies on the efficient spatial charge separation for broad solar light absorption and water remediation have been a major priority. Moreover, the development of transition metal-doped nanocomposites for this purpose is a new endeavor in current research. Here, we constructed an Fe<sup>3+</sup>-doped CdO/ZnS nanocomposite with a low doping level and investigated the effect of doping on the charge transfer and recombination behavior for improved photocatalytic performance. The X-ray diffraction analysis results indicate that both materials, CdO and ZnS, exhibit a cubic phase structure with an average crystallite size of 35 nm. Morphology analysis of the Fe<sup>3+</sup>-doped CdO/ZnS nanocomposite confirms the formation of irregularly shaped particle-like structures. From the optical studies, the bandgap energies of CdO/ZnS and Fe<sup>3+</sup>-doped CdO/ZnS nanocomposites are 3.19 eV and 2.87 eV, respectively, which proved that the iron ions doping reduced the bandgap energy and extended the absorption to the visible range. The efficiency of photodegradation in the tested samples was evaluated using tetracycline under solar light exposure. The experimental results demonstrated that the Fe<sup>3+</sup>-doped CdO/ZnS nanocomposite outperformed the other samples, exhibiting a significantly higher photocatalytic activity. After 80 min, it achieved a remarkable degradation rate of 97.06%. The Fe<sup>3+</sup>-doped CdO/ZnS nanocomposite demonstrated good stability and recyclability after five cycles. Radical trapping experiments showed that hydroxyl (•OH) radicals play a key role in photodegradation.

**Keywords:** CdO/ZnS; Fe<sup>3+</sup> ions doping; solar light; tetracycline; photocatalysis



**Citation:** Stella, R.J.; Sreevani, I.; Gurugubelli, T.R.; Ravikumar, R.V.S.S.N.; Koutavarapu, R. Enhanced Solar Light-Driven Photocatalytic Degradation of Tetracycline Using Fe<sup>3+</sup>-Doped CdO/ZnS Nanocomposite: Mechanistic Insights and Performance Evaluation. *Catalysts* **2023**, *13*, 1312. <https://doi.org/10.3390/catal13091312>

Academic Editor: Juan Matos Lale

Received: 3 September 2023

Revised: 19 September 2023

Accepted: 20 September 2023

Published: 21 September 2023



**Copyright:** © 2023 by the authors. Licensee MDPI, Basel, Switzerland. This article is an open access article distributed under the terms and conditions of the Creative Commons Attribution (CC BY) license (<https://creativecommons.org/licenses/by/4.0/>).

## 1. Introduction

In recent times, environmental pollution has emerged as a worldwide concern. Aquatic environments, in particular, have become a repository for a range of diverse compounds, which are collectively known as emerging pollutants [1,2]. This intriguing category has attracted intense attention because of its potential ramifications for both ecological integrity and human well-being. Notably, a significant subset of these compounds exhibits remarkable resilience against conventional chemical oxidation methods. Furthermore, their inherent toxicity poses formidable obstacles to successful biodegradation processes. Consequently, the possibility of their release into the environment is a worrying conundrum [3,4]. In recent decades, there has been a notable surge in the demand for pharmaceutical products in developing nations, encompassing a spectrum of categories including analgesics,

antibiotics, anti-inflammatory agents, lipid regulators, beta blockers, and tranquilizers [5,6]. Significant proportions of these pharmaceutical compounds exhibit robust stability, posing considerable challenges for their effective dismantling through conventional wastewater treatment methodologies [7]. Consequently, a substantial presence of these pharmaceutical compounds is consistently observed across diverse water sources, including sewage and surface water, as well as within drinking water, groundwater, soil, sediments, and sludge [8].

Tetracycline (TC) is a globally utilized antibiotic known for its extensive range of effectiveness. It proves to be effective against infections caused by both Gram-positive and Gram-negative microorganisms [9]. Moreover, TC is used in the medical, veterinary and agricultural fields due to its low cost and high antimicrobial activity [10]. Hence, the emergence of antibiotics within aquatic ecosystems is entwined with an array of adverse outcomes, encompassing short-term and protracted toxicity, the perturbation of endocrine systems, and the proliferation of antibiotic-resistant bacterial strains [11]. Therefore, it is necessary to find an effective solution to remove it from the water environment. In recent times, the use of solar light-based photochemical reactions using advanced oxidation processes (AOPs) has gained importance. These processes facilitate the conversion of a variety of harmful contaminants into benign by-products and offer the remarkable feature of complete environmental friendliness [12,13]. A key aspect of AOPs involves photocatalytic mechanisms, in which semiconductor-mediated reactions are catalyzed upon exposure to light. As such, these photocatalytic processes hold considerable promise in mitigating the dual controversies of energy scarcity and environmental pollutants across a broad spectrum of solar radiation [14,15].

Semiconductor nanomaterials have attracted considerable interest in the research field due to their ability to exhibit superior properties compared to their conventional counterparts. Currently, growing interest is directed toward semiconductor nano-photocatalysts, which is a phenomenon driven by the advent of innovative synthesis methods and an ever-expanding landscape of applications [16,17]. To overcome this limitation, a series of strategies to enhance the solar light absorption capabilities of semiconductor photocatalysts have been meticulously explored [18,19]. Doping and semiconductor coupling are widely employed techniques to enhance the activity, selectivity, and stability of photocatalysts while reducing their bandgap [20]. These strategies include the introduction of transition metal ions through doping, sensitizing catalyst surfaces, and judicious modification of the catalyst's surface properties. In concert, these methods have the potential to increase the efficiency of photocatalysis by utilizing a broad spectrum of solar illumination [21,22].

Semiconductor nanocomposites serve as key structural frameworks in the fabrication of photocatalytic materials. A concerted alignment of the conduction band (CB) and valence band (VB) in heterogeneous semiconductor materials is an imperative requirement for the construction of heterostructures [23]. Extensive investigations have been conducted on various metal oxide semiconductors, including ZnO, MgO, CuO, WO<sub>3</sub>, and CdO, owing to their narrower bandgap, lower toxicity, and exceptional thermal and chemical stability [24,25]. Among these, CdO is an emerging material attracting research attention owing to its narrow bandgap energy and high thermal and chemical stability [26]. Because of its affordability and exceptional thermal and chemical stability, it has gained popularity as a photocatalyst. Nevertheless, its photocatalytic efficiency remains relatively low due to its limited responsiveness to visible light and the rapid recombination of charge carriers [27]. Thus, combining two or more semiconductors to form a nanocomposite is the most effective strategy to overcome these limitations [28,29]. ZnS is a highly functional material with outstanding physical and chemical properties. It is an economical, non-toxic, and exceptionally biocompatible material. This semiconductor is noteworthy for its direct bandgap of 3.5 eV and holds substantial importance in energy and environmental applications [30,31]. Consequently, the development of a CdO/ZnS nanocomposite holds the potential for highly efficient catalytic performance in pollutant degradation. The creation of a heterostructure

with robust synergistic interactions can significantly diminish recombination rates while harnessing solar light effectively, thereby preserving a high redox capacity [32].

Moreover, doping plays a crucial role in enhancing the photocatalytic properties of semiconductors by altering the electronic configuration of materials, resulting in the generation of an excess of defect energy levels [33]. In order to enhance the photocatalytic properties of CdO/ZnS nanocomposite, transition metal ions doping is frequently applied. Thus, in this work, we fabricated a CdO/ZnS nanocomposite with a low doping content of  $\text{Fe}^{3+}$  ions and applied it to tetracycline degradation. The main active substances were explored by radical trapping experiments, and the photostability of the materials was evaluated by cycling experiments. Therefore, the  $\text{Fe}^{3+}$ -doped CdO/ZnS nanocomposite research can provide additional references for the development of efficient and stable semiconductor photocatalysts.

## 2. Results and Discussion

### 2.1. Structural Analysis

The X-ray diffraction (XRD) pattern of  $\text{Fe}^{3+}$ -doped CdO/ZnS nanocomposite is shown in Figure 1. The XRD spectrum reveals two material phases, CdO (\*) and ZnS (#); both exhibit the cubic phase of the material, and these patterns align with JCPDS file No. 05-0640 and 05-0566, respectively [34,35]. In the presented spectrum, a high intense peak is observed at  $2\theta = 32.58^\circ$  analogous to the (111) plane, which is the indication of the crystalline phase of CdO belonging to unit cell parameter  $a = 0.4733$  nm for the cubic phase. ZnS, like CdO, is a cubic phase with  $a = 0.5373$  nm as a unit cell parameter. From the well-known Scherrer equation, the crystallite size is approximated as 35 nm [36]. The inset of Figure 1 shows the magnified XRD image of undoped and  $\text{Fe}^{3+}$ -doped CdO/ZnS nanocomposites. A slight change in  $2\theta$  values was observed, indicating the doping of  $\text{Fe}^{3+}$  ions in the CdO/ZnS nanocomposite [37].

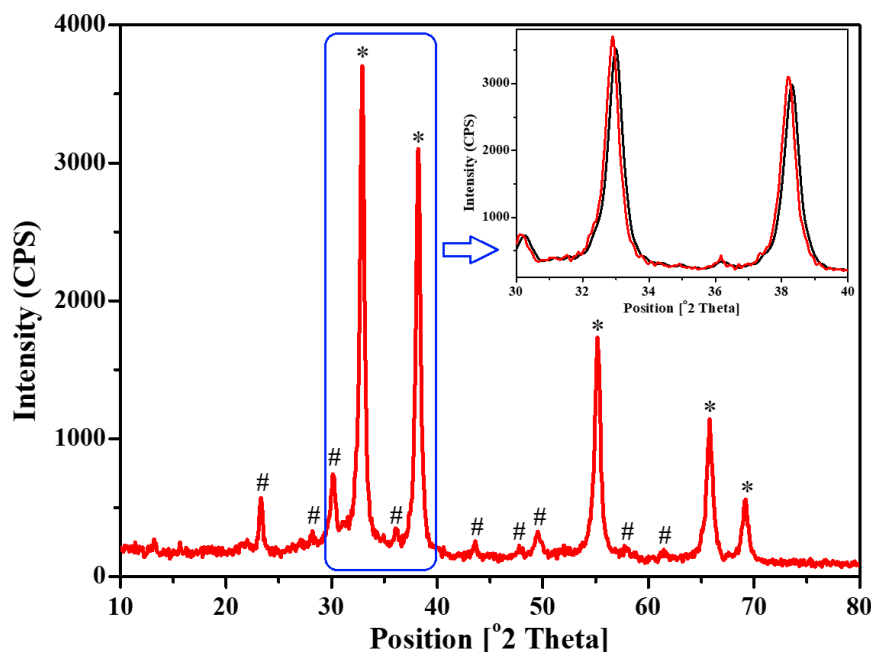


**Figure 1.** XRD pattern of  $\text{Fe}^{3+}$ -doped CdO/ZnS nanocomposite, and insert shows the magnified image of undoped and  $\text{Fe}^{3+}$ -doped CdO/ZnS nanocomposites. CdO (\*) and ZnS (#).

### 2.2. Morphological Analysis

Morphological analyses of the fabricated heterostructure were conducted using SEM, TEM, and HRTEM. In Figure 2, SEM images are utilized to depict the morphology of the  $\text{Fe}^{3+}$ -doped CdO/ZnS nanocomposite. These images, captured at two different magnifications, reveal a dispersion of spherical nanoparticles with some agglomeration.

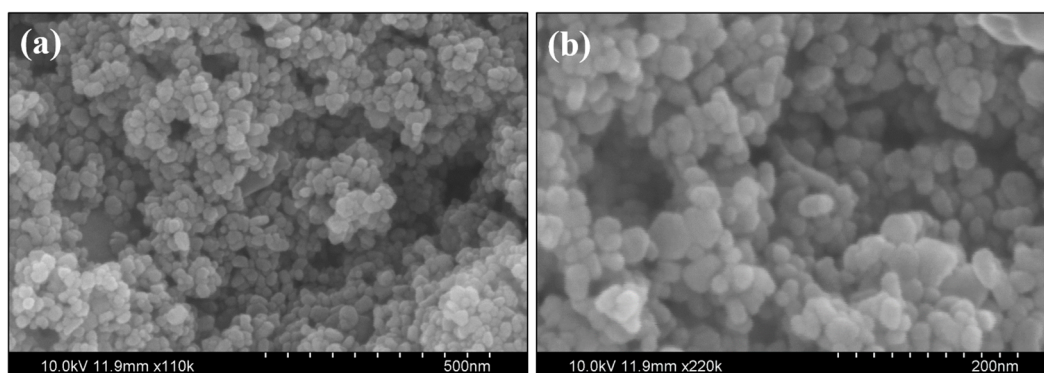


**Figure 2.** (a,b) SEM images of  $\text{Fe}^{3+}$ -doped CdO/ZnS nanocomposite.

Figure 3a,b present TEM and HRTEM images of the  $\text{Fe}^{3+}$ -doped CdO/ZnS nanocomposite, confirming the formation of irregularly shaped particle-like structures. In Figure 3c, the observed lattice spacings of 0.265 nm and 0.306 nm correspond to the (111) plane of CdO and the (111) plane of ZnS, respectively, indicating the formation of a CdO/ZnS heterostructure [38,39]. Furthermore, the diffraction spots in the corresponding Selected Area Electron Diffraction (SAED) pattern in Figure 3d confirm the simultaneous presence of CdO and ZnS.

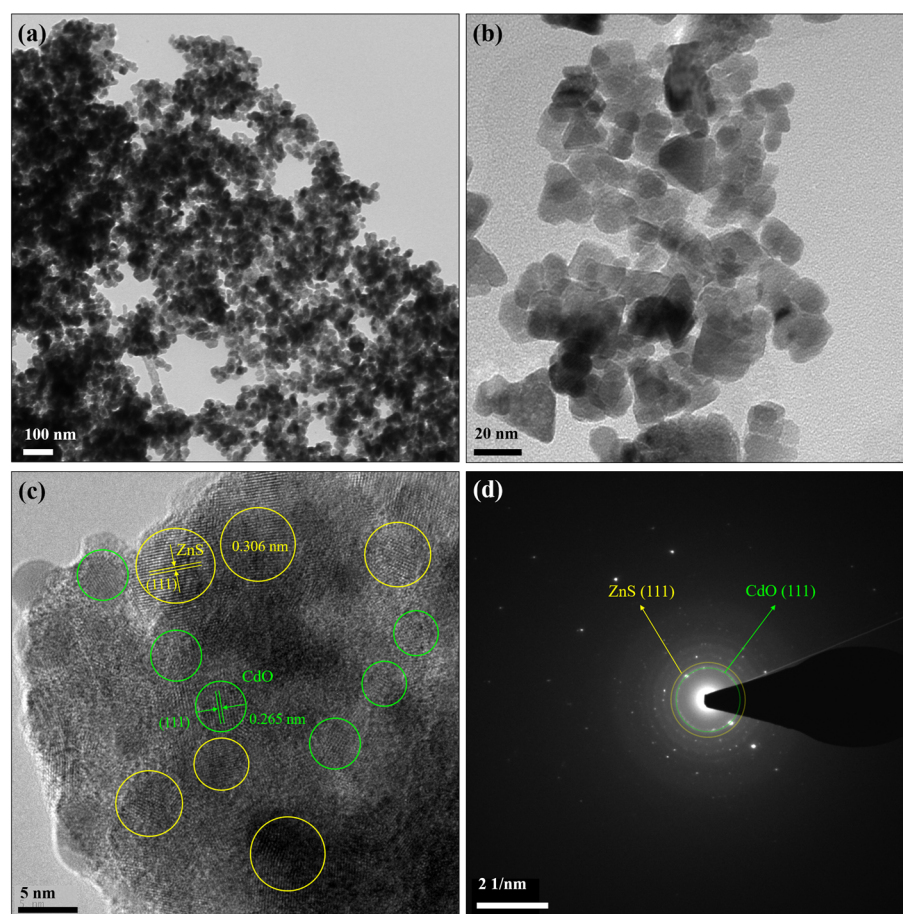


**Figure 3.** (a) TEM, (b) HRTEM, (c) lattice fringe, and (d) SAED pattern of  $\text{Fe}^{3+}$ -doped CdO/ZnS nanocomposite.

To further understand the elemental composition of the composite, Energy-Dispersive X-ray Spectroscopy (EDS) was employed. Figure S1 confirmed the compositional analysis

of the prepared sample. Figure 4 illustrates the distribution of surface elements such as Cd, Zn, O, S, and Fe across the sample, indicating uniform distribution throughout the material.

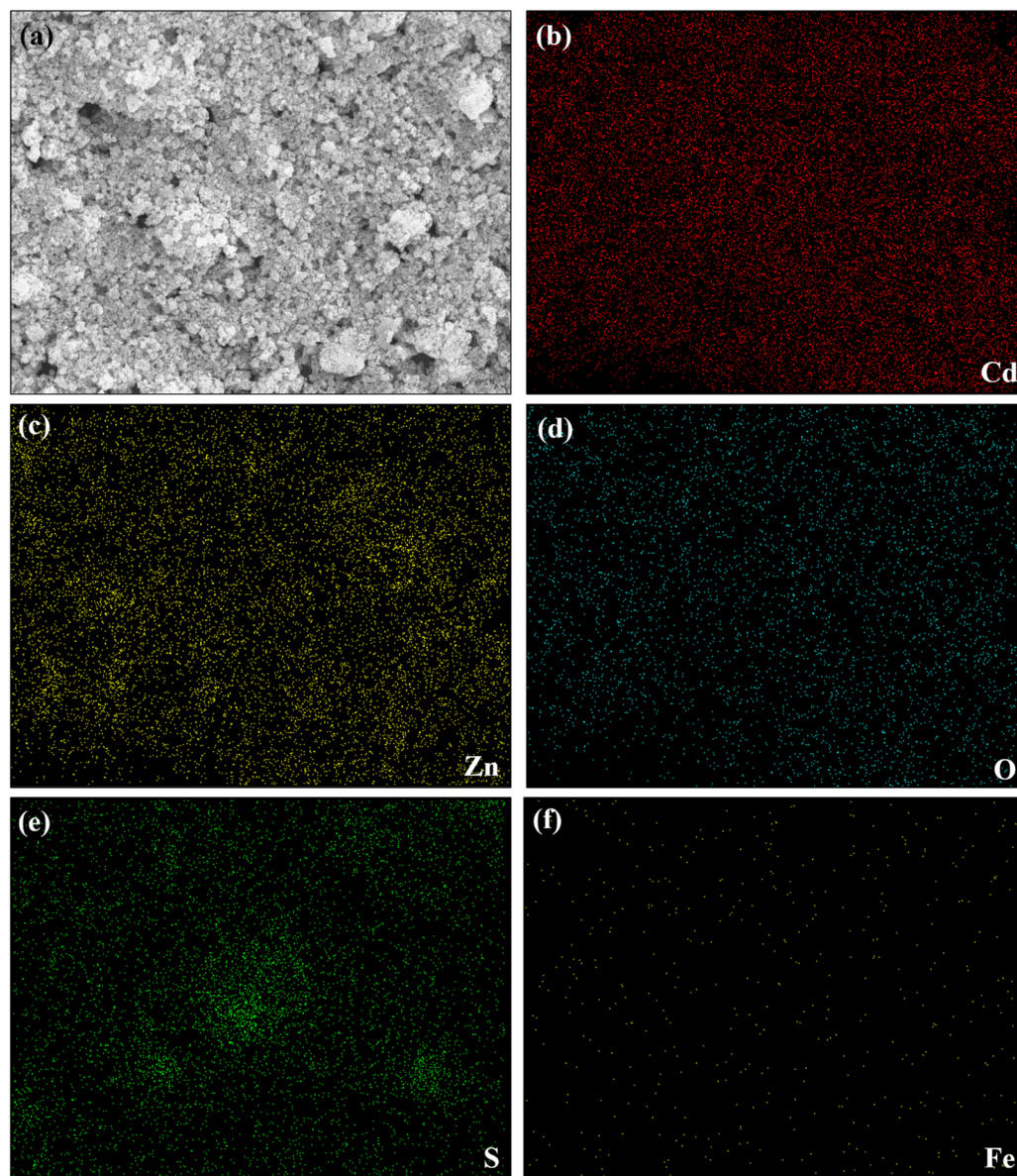


**Figure 4.** EDS color mapping of  $\text{Fe}^{3+}$ -doped CdO/ZnS nanocomposite. (a) Mapping region, (b) Cd, (c) Zn, (d) O, (e) S, and (f) Fe.

### 2.3. Elemental Composition Analysis

A survey scan using X-ray Photoelectron Spectroscopy (XPS) analysis was conducted to determine the elements and interactions between CdO, ZnS and doped  $\text{Fe}^{3+}$  ions present in the  $\text{Fe}^{3+}$ -doped CdO/ZnS nanocomposite. Figure 5 presents the XPS analysis of the  $\text{Fe}^{3+}$ -doped CdO/ZnS nanocomposite. The XPS full spectrum in Figure 5a reveals the presence of elements including S, Cd, O, Fe, and Zn. Additionally, the sample exhibits a distinct Fe 2p signal, confirming the successful doping of  $\text{Fe}^{3+}$  ions. In Figure 5b, the S 2p spectrum is fitted with two peaks at 161.28 eV and 162.47 eV, corresponding to S 2p<sub>3/2</sub> and S 2p<sub>1/2</sub>, respectively. These peaks are characteristic of the  $\text{S}^{2-}$  state [40]. In Figure 5c, the XPS spectrum reveals two distinct peaks at 404.95 eV and 411.75 eV, which correspond to Cd 3d<sub>5/2</sub> and Cd 3d<sub>3/2</sub> of Cd 3d, respectively. These peaks are characteristic of  $\text{Cd}^{2+}$  in CdS [41]. After deconvolution, the XPS spectrum of O 1s in Figure 5d exhibits two distinct

peaks. The peak at 530.41 eV is attributed to oxygen-deficient regions within the CdO matrix. Meanwhile, the peak at 532.07 eV is often associated with chemically adsorbed oxygen species on the surface of CdO [42]. In Figure 5e, the Fe 2p spectrum exhibits two distinct peaks at 709.95 eV for Fe 2p<sub>3/2</sub> and at 724.08 eV for Fe 2p<sub>1/2</sub> [43]. Additionally, the Zn 2p XPS spectrum in Figure 5f displays peaks corresponding to Zn 2p<sub>3/2</sub> and Zn 2p<sub>1/2</sub> at 1022.24 eV and 1045.32 eV, respectively. These peaks indicate the presence of Zn with a +2 oxidation state [44]. Overall, the XPS analysis confirms a significant interaction between the elements, which enhances synergistic effects and facilitates the efficient transfer of charge carriers within the nanocomposite.

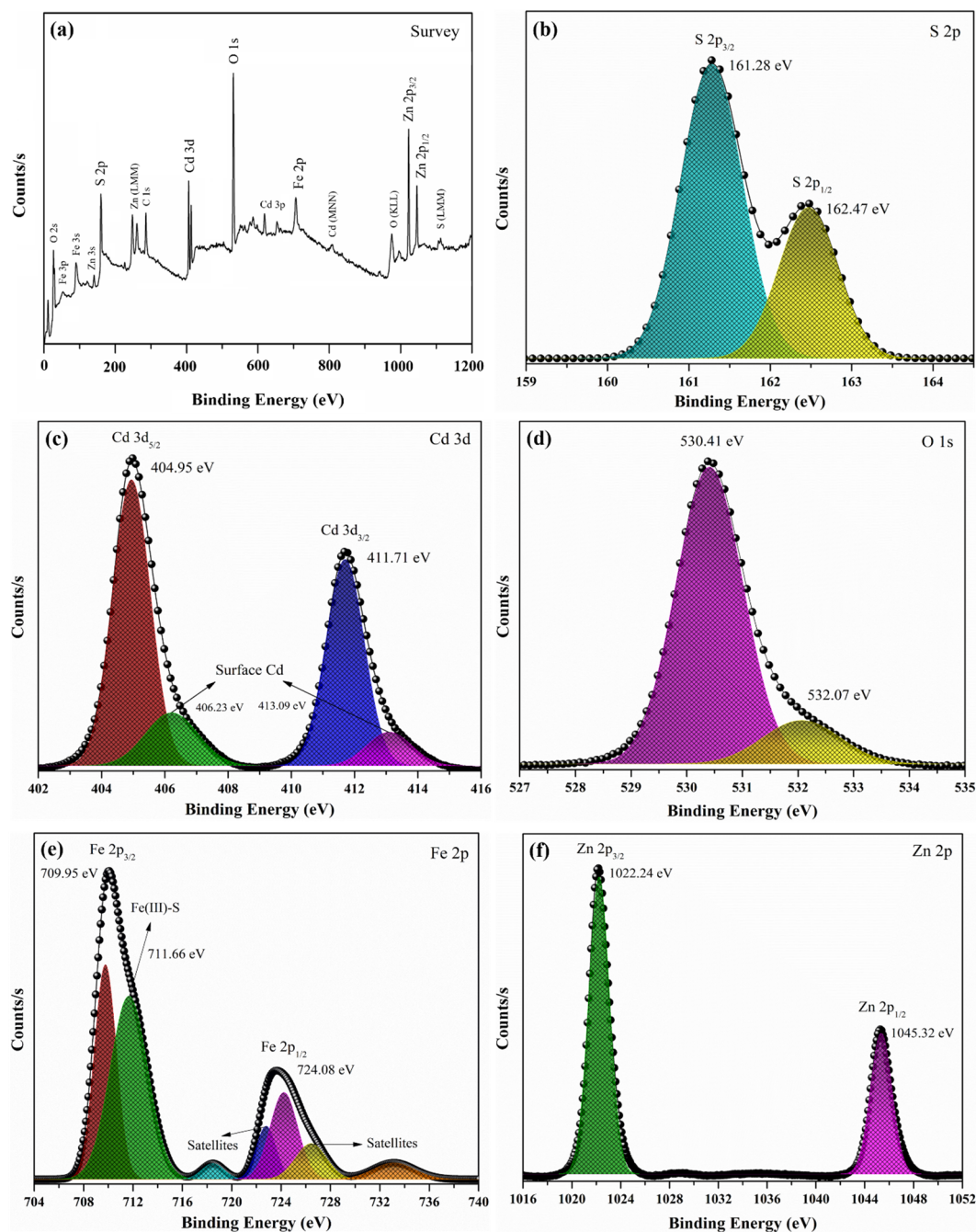


**Figure 5.** XPS analysis of Fe<sup>3+</sup>-doped CdO/ZnS nanocomposite. (a) Survey spectrum, (b) S 2p, (c) Cd 3d, (d) O 1s, (e) Fe 2p, and (f) Zn 2p.

#### 2.4. Optical Absorption and EPR Analysis

The UV-vis Diffuse Reflectance Spectroscopy (DRS) spectra of both the CdO/ZnS and Fe<sup>3+</sup>-doped CdO/ZnS nanocomposites are presented in Figure 6a. In this figure, the CdO/ZnS nanocomposite exhibits a pronounced ultraviolet light absorption response, which is characterized by an absorption edge at approximately 389 nm. However, the Fe<sup>3+</sup>-doped CdO/ZnS nanocomposite exhibits better visible light absorption compared to CdO/ZnS with an absorption edge around 432 nm. Thus, it can be seen that the doping of Fe<sup>3+</sup> ions improved the light utilization efficiency of the Fe<sup>3+</sup>-doped CdO/ZnS nanocomposite. The bandgaps of both photocatalysts were determined using Tauc plots, and the results are presented in Figure 6b. The bandgap of the CdO/ZnS nanocomposite is calculated to be 3.19 eV, while the Fe<sup>3+</sup>-doped CdO/ZnS nanocomposite exhibits a reduced bandgap of 2.87 eV. Furthermore, the band edge positions of CdO and ZnS were calculated using well-established standard empirical formulas [45]. For CdO, the valence band (VB) edge position is +2.56 eV, the conduction band (CB) edge position is +0.17 eV, and the bandgap is 2.39 eV. In the case of ZnS, the valence band edge position is +2.39 eV, the conduction band edge position is −1.08 eV, and the bandgap is 3.47 eV.

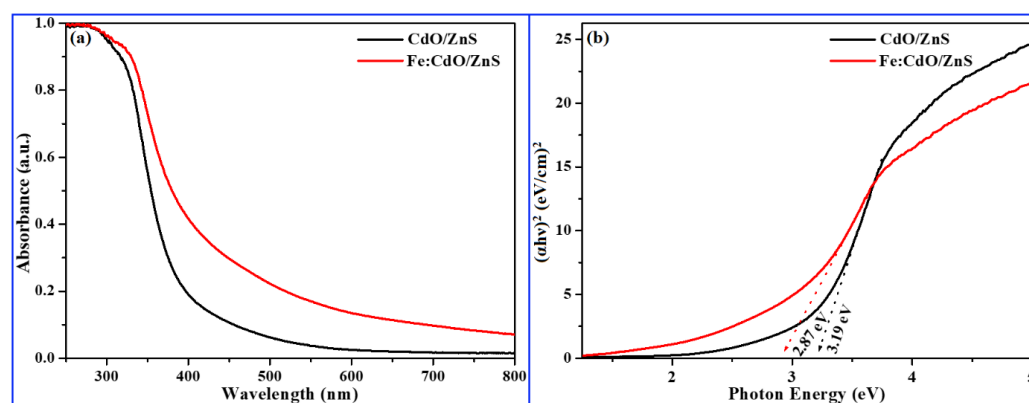


**Figure 6.** (a) DRS, (b) Tauc plots of undoped and Fe<sup>3+</sup>-doped CdO/ZnS nanocomposite.

To gain more comprehensive insights into the impact of Fe<sup>3+</sup>-doping on the photocatalytic reaction, the efficiency of charge migration and transfer was assessed through excitation-dependent photoluminescence (PL) spectra. This analysis provides valuable information closely linked to the photocatalytic performance of the samples. In general, it is beneficial to increase the level of PL intensity quenching to improve the photocatalytic efficiency. The PL spectra of CdO/ZnS and Fe<sup>3+</sup>-doped CdO/ZnS nanocomposites are presented in Figure 7a. As shown, the PL spectrum of CdO/ZnS exhibits a strong PL emission peak originating from its intense charge carrier recombination. The Fe<sup>3+</sup>-doped CdO/ZnS nanocomposite, when subjected to the same excitation wavelength (325 nm), displays a notably lower PL peak compared to CdO/ZnS. This difference can be attributed to the intimate interfacial contact between the doped Fe<sup>3+</sup> ions and the host sites. Consequently, the creation of interfacial contact and the introduction of defect energy levels play a crucial role in significantly extending the lifetime of electron–hole pairs. This extended lifetime is highly advantageous for promoting efficient photocatalytic reactions [46].

Figure 7b shows the Electron Paramagnetic Resonance (EPR) spectrum of the Fe<sup>3+</sup>-doped CdO/ZnS nanocomposite at room temperature. In weak crystal fields, Fe<sup>3+</sup> has five unpaired electrons, bringing about a high-spin state (<sup>6</sup>S<sub>5/2</sub>). Since Fe<sup>3+</sup> has a d<sup>5</sup> arrangement, it has <sup>6</sup>S. The g-factor is relied upon to be amazingly near the free particle value of 2.0023 in light of the fact that there is no twist circle connection. The strong signals at g~2 and a shoulder at g~3 districts rule the EPR range in this investigation. The reverberation signal at g~2.09 shows up initially when iron is readily available in the host cross-section at misshaped octahedral site consistency. The spin minute of covalently linked Fe<sup>3+</sup> ions may be minimized as a result of the shift from a high-spin to a low-spin

$\text{Fe}^{3+}$  state, potentially leading to the creation of a new resonance signal  $g \sim 3.015$  [47]. The effective  $g$ -factor of the broad signal is greater than 2.0023, suggesting the presence of iron ions in the sample.

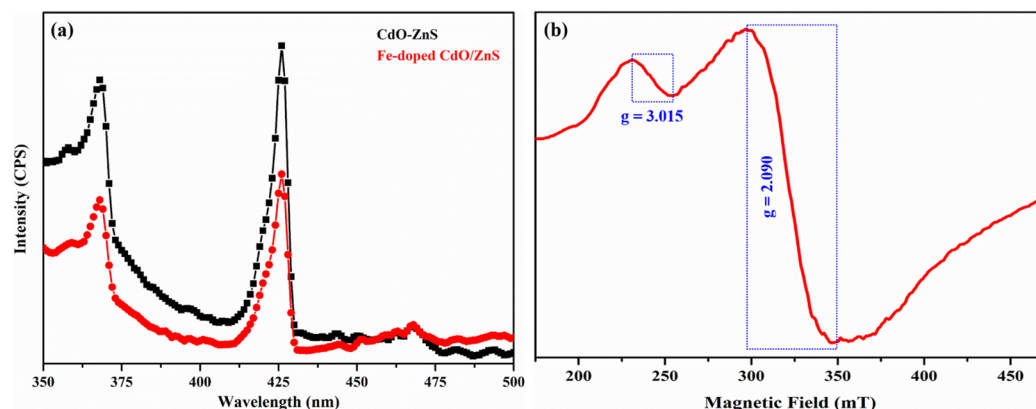


**Figure 7.** (a) PL spectra of undoped and  $\text{Fe}^{3+}$ -doped CdO/ZnS nanocomposite, and (b) EPR spectrum of  $\text{Fe}^{3+}$ -doped CdO/ZnS nanocomposite.

### 2.5. Photocatalytic Performance

The assessment of the catalyst's photocatalytic activity was determined by measuring the degradation rates of TC under solar light, and the outcomes are presented in Figure 8. In the absence of a photocatalyst, the photodegradation of TC remained negligible even after 80 min of exposure. Figure 8a illustrates the reduction in the absorption peak intensity of TC at 351 nm as a function of increasing irradiation time up to 80 min. After illumination for 80 min, ZnS, CdO, and CdO/ZnS showed the lower photocatalytic performance with degradation efficiencies of 20.27%, 35.13% and 68.41%, respectively. Furthermore, the  $\text{Fe}^{3+}$ -doped CdO/ZnS nanocomposite exhibited the strongest photocatalytic activity and arrived at the optimum photocatalytic degradation activity (97.06%) after 80 min (Figure 8b). To assess the degradation kinetics, the pseudo-first-order kinetic model was employed to describe the photocatalytic performance of the synthesized samples. The results of this analysis are presented in Figure 8c. The degradation kinetic rate constants of ZnS, CdO, and CdO/ZnS were found to be 0.003, 0.0057, and 0.0142  $\text{min}^{-1}$ , respectively, while the degradation kinetic rate constant of the  $\text{Fe}^{3+}$ -doped CdO/ZnS nanocomposite was found to be 0.0341  $\text{min}^{-1}$  (Figure 8d). The kinetic rate constants of photodegradation of TC on the  $\text{Fe}^{3+}$ -doped CdO/ZnS nanocomposite increased the rate by approximately 11.37, 5.98, and 2.41 times over ZnS, CdO and CdO/ZnS, respectively.

The impact of catalyst dosage was examined by varying the amounts (10, 15, and 20 mg) of the  $\text{Fe}^{3+}$ -doped CdO/ZnS nanocomposite. As depicted in Figure 9a, the photodegradation of TC gradually increases with the rising catalyst loading until it reaches 15 mg. This increase can be attributed to the greater availability of active sites and the enhanced production of active radicals. However, when the catalyst dosage exceeds 15 mg, the suspended catalyst particles tend to aggregate. This aggregation reduces the amount of light that can access the active sites of the catalyst, subsequently decreasing the rate of photodegradation. Furthermore, the stability experiment was performed to understand the cyclic stability of the  $\text{Fe}^{3+}$ -doped CdO/ZnS nanocomposite (Figure 9b). The stability test results inferred that the photodegradation efficiency of TC slowly decreased from the 1st cycle to the 5th cycle and finally stabilized around at 92.16%. Thus, the degradation efficiency of the  $\text{Fe}^{3+}$ -doped CdO/ZnS nanocomposite reduced slightly after the cycle experiment, which may be attributed to the loss of catalyst and the decrease in active sites in the samples during the cycle experiments [48].

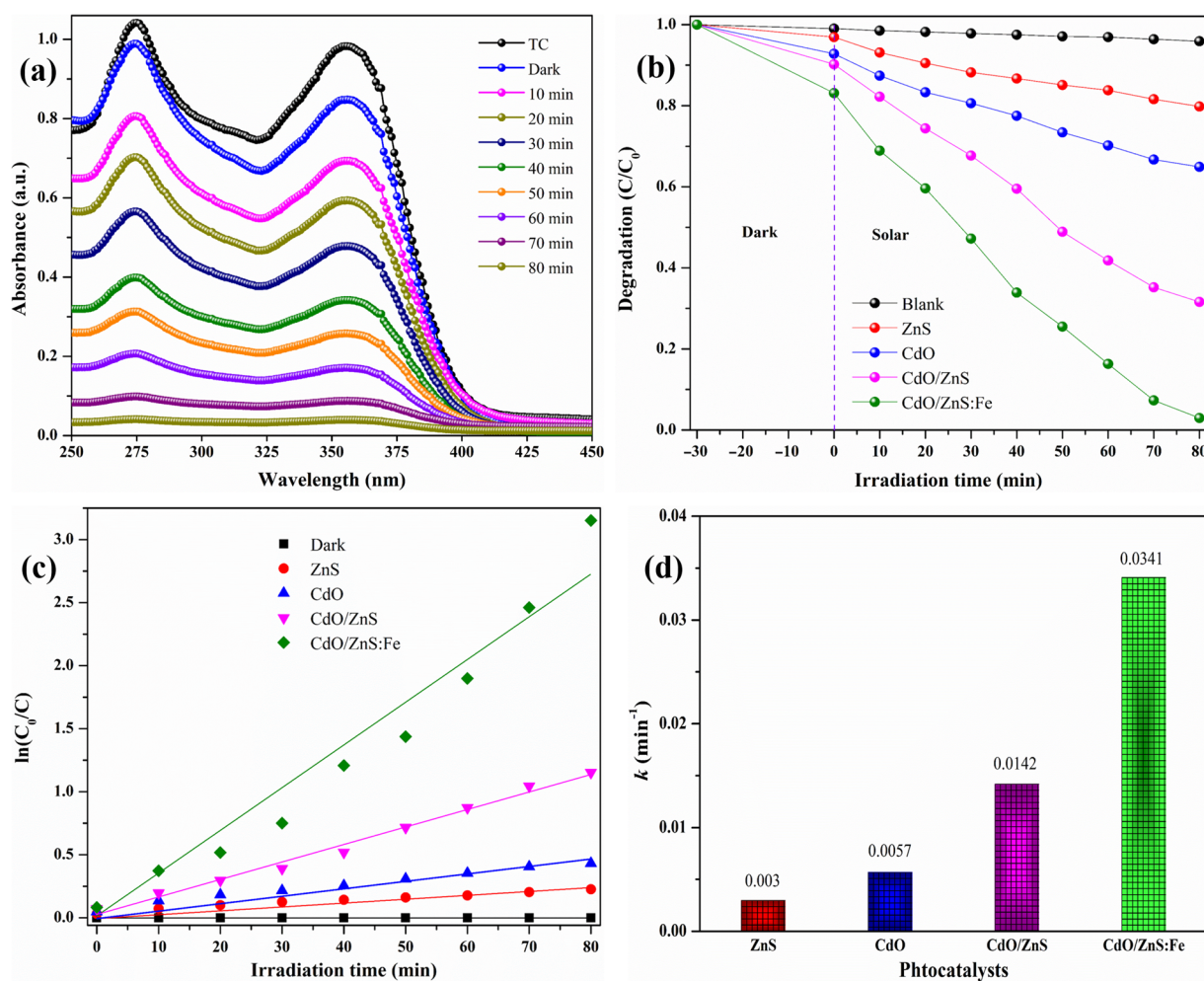


**Figure 8.** (a) Absorption spectrum of TC degradation over  $\text{Fe}^{3+}$ -doped CdO/ZnS nanocomposite, (b) photocatalytic activity, (c)  $\ln$  graph, and (d) rate constants of all prepared samples.

Furthermore, a comprehensive characterization of the crystallinity and morphology of the  $\text{Fe}^{3+}$ -doped CdO/ZnS nanocomposite was performed after multiple recycling cycles using SEM and TEM, the results of which are presented in Figures S2 and S3. These results indicate that there are no noticeable changes in the crystallinity and morphology of the  $\text{Fe}^{3+}$ -doped CdO/ZnS nanocomposite after cycle tests. Identifying the key reactive species ( $\bullet\text{O}_2^-$ ,  $\bullet\text{OH}$ , and  $h^+$ ) critical to the photocatalytic removal process is crucial to fully understand the photocatalytic mechanism. To learn more about this, benzoquinone (BQ for  $\bullet\text{O}_2^-$  scavenger), isopropanol (IPA for  $\bullet\text{OH}$  scavenger), and triethanolamine (TEOA for  $h^+$  scavenger) were added to the reaction solution during TC degradation on the  $\text{Fe}^{3+}$ -doped CdO/ZnS nanocomposite. The photodegradation rates of TC versus the  $\text{Fe}^{3+}$ -doped CdO/ZnS nanocomposite with and without scavengers were examined and are shown in Figure 9c,d. As observed, the degradation efficiency of the composite for TC showed a slight reduction when BQ was added (83.74%), which was followed by TEOA (75.46%). This suggests that  $\bullet\text{O}_2^-$  radicals and holes played a relatively minor role in the photocatalytic reaction. However, the addition of IPA resulted in the lowest degradation efficiency (28.67%) of TC by the  $\text{Fe}^{3+}$ -doped CdO/ZnS nanocomposite, indicating that  $\bullet\text{OH}$  radicals played a significant role in the photocatalytic reaction. This highlights that the primary reactive species responsible for the degradation of TC is the  $\bullet\text{OH}$  radical. The catalytic removal of TC in the present work is compared with that previously reported in the literature, as shown in Table 1 [49–58]. The data reveal the enhanced photocatalytic activity of the  $\text{Fe}^{3+}$ -doped CdO/ZnS nanocomposite.

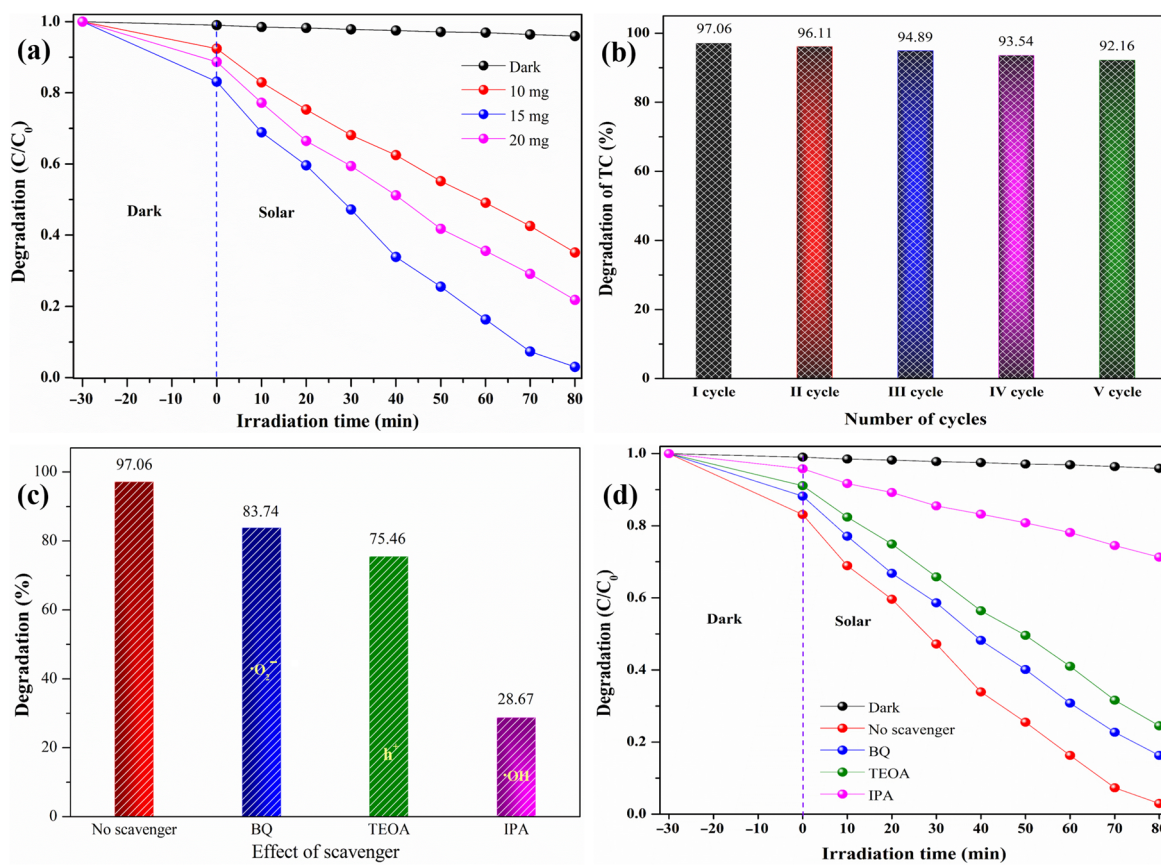


**Figure 9.** (a) Catalyst loading, (b) stability, and (c,d) scavenger test for Fe<sup>3+</sup>-doped CdO/ZnS nanocomposite.

**Table 1.** A comparison of photocatalytic removal of pollutants under light illumination with recent literature.

S.No.	Catalysts	Synthesis Technique	Pollutant	Light Source	Irradiation Time (min)	Degradation Efficiency (%)	Ref.
1	ZnO/SnS	Hydrothermal	MB	Visible	210	95.20	[49]
2	CdO/CuO	Microwave	RB	Solar	120	97.00	[50]
3	ZnO-CdS	Chemical precipitation	RhB	Solar	80	98.16	[51]
4	ZnO/CdS	Wet chemical	RhB	Solar	80	90.00	[52]
5	Fe-dope ZnO/CdS	Chemical	MB	Visible	80	78.00	[53]
6	Cu-doped ZnO/SnS	Hydrothermal	MB	Solar	120	97.20	[54]
7	Fe-doped ZnO/SnS	Hydrothermal	MB	Visible	120	95.80	[55]
8	Dy-doped ZnO/SnS	Hydrothermal	MB	Visible	140	97.80	[56]
9	V-doped ZnO/SnS	Hydrothermal	MB	Visible	120	96.40	[57]
10	Cu-doped TiO <sub>2</sub> /ZnO	Sol-gel	MB	Visible	120	73.20	[58]
11	Fe-doped CdO/ZnS	Hydrothermal	TC	Solar	80	97.06	Present work

Based on the experimental findings and analysis, the potential photodegradation mechanism and photoinduced charge transfer during TC degradation by the Fe<sup>3+</sup>-doped CdO/ZnS nanocomposite are illustrated in Figure 10. When the photocatalyst is exposed

to solar radiation, it generates pairs of electrons and holes on its surface. Furthermore, the introduction of iron ions through doping creates defect energy states below the CB of ZnS. These defect levels act as traps for the charge carriers generated upon exposure to light, reducing electron–hole recombination and facilitating their migration to the surface of the catalyst. Following light illumination, the excited electrons transition from the CB of ZnS and defect energy levels to the CB of CdO, while the holes move from the VB of CdO to the VB of ZnS. The negative charge carriers that accumulate on the surface of CdO may interact with  $O_2$  to generate  $\bullet O_2^-$  radicals and  $H_2O_2$ , which subsequently induce the formation of  $\bullet OH$  radicals. On the other hand, the direct contribution of holes on the ZnS surface in the oxidation process of TC produces  $\bullet OH$  radicals as well. Based on these observations, the  $Fe^{3+}$ -doped nanocomposite effectively separates the photoinduced  $e^-/h^+$  pairs and generates robust oxidative free radicals on the photocatalysts surface, leading to a significant enhancement in photodegradation efficiency.

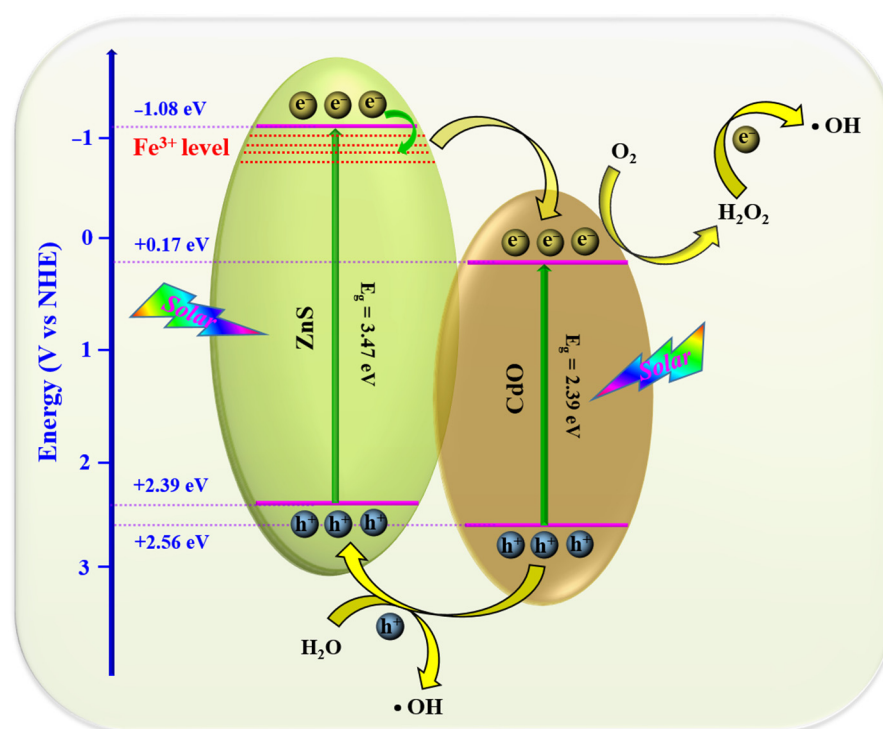


**Figure 10.** Photocatalytic mechanism for the degradation of tetracycline over  $Fe^{3+}$ -doped CdO/ZnS nanocomposite.

### 3. Materials and Methods

#### 3.1. Materials

The chemical precursors, including cadmium acetate, sodium hydroxide, zinc acetate, sodium sulfide, iron nitrate, benzoquinone, triethanolamine, and isopropyl alcohol, were acquired from Sigma-Aldrich and used in their as-received state without additional purification.

#### 3.2. Fabrication of $Fe^{3+}$ -doped CdO/ZnS Nanocomposite

The  $Fe^{3+}$ -doped CdO/ZnS nanocomposites were created using a direct hydrothermal method. In the beginning, 25 mL of deionized (DI) water was used to dissolve 0.2 mol of cadmium acetate, sodium hydroxide, zinc acetate, and sodium sulfide individually. The procedure began with the gradual addition of a NaOH solution to the cadmium solution with constant agitation. This resulted in the formation of CdO, which was evident from the homogenous precipitate formed. To synthesize ZnS nanoparticles, a  $Na_2S$  solution was slowly introduced into the zinc solution. Subsequently, 20 mL of a 0.01 mol iron

nitrate solution was added to the ZnS mixture and stirred for 30 min, indicating the formation of Fe<sup>3+</sup>-doped ZnS nanostructures. In order to create the Fe<sup>3+</sup>-doped CdO/ZnS nanocomposites, the Fe<sup>3+</sup>-doped ZnS precipitate was lastly mixed with the CdO precipitate. The resulting solution was transferred into an autoclave and heated to 180 °C for a duration of 12 h after 30 min of continuous stirring. Subsequently, the resulting products were allowed to cool naturally to room temperature, which was followed by filtration and washing with DI water and ethanol. The settled product was then dried overnight at 80 °C. The resulting test material was ground and employed for further characterization and the study of TC degradation under solar light exposure.

### 3.3. Characterizations

X-ray diffraction analysis was conducted using a Shimadzu 6100 X-ray diffractometer equipped with Cu K $\alpha$  radiation. Field emission scanning electron microscopy (FESEM) images and energy-dispersive X-ray spectra of the prepared samples were acquired using a HITACHI S-4800 system. Transmission electron microscopy (TEM) images were obtained using a HITACHI H-7600 electron microscope, while high-resolution transmission electron microscopy (HRTEM) images were captured with a Tecnai G2 F20 S-Twin electron microscope. X-ray Photoelectron Spectroscopy (XPS) data were collected using a Thermo Scientific K $\alpha$  X-ray source. UV-vis diffuse reflectance spectra were recorded using a VARIAN Cary 5000 spectrophotometer. Photoluminescence spectra of the catalysts were measured using a Horiba IHR550 fluorescence spectrophotometer.

### 3.4. Photocatalytic Test

The photocatalytic effectiveness of the as-prepared samples was assessed for the degradation of TC under solar light exposure. Typically, 15 mg of Fe<sup>3+</sup>-doped CdO/ZnS photocatalyst was introduced into a 50 mL TC aqueous solution (40 mg/L) and subjected to 2 min of sonication to ensure uniform mixing. Before initiating the illumination, the reaction mixture was vigorously stirred in the dark for 30 min to establish an adsorption–desorption equilibrium. Subsequently, the suspension mentioned above was exposed to solar light. The photocatalytic performance of the prepared catalysts was evaluated using a 150 W solar simulator. Meanwhile, at specified time intervals, 3 mL of the reaction suspensions was collected and separated by centrifugation.

## 4. Conclusions

In conclusion, the Fe<sup>3+</sup>-doped CdO/ZnS nanocomposite was fabricated by incorporating a low amount of iron ions doping. XRD analysis revealed the cubic crystal structure of the prepared sample. The bandgap energies of CdO/ZnS and Fe<sup>3+</sup>-doped CdO/ZnS nanocomposites are 3.19 eV and 2.87 eV, respectively. The morphological study confirmed the formation of irregular shaped nanoparticles, and elemental analysis affirms the presence of Cd, O, Zn, S, and Fe species. XPS analysis confirms a significant interaction between the elements, which enhances synergistic effects and the easy transfer of charge carriers. From PL analysis, the Fe<sup>3+</sup>-doped CdO/ZnS nanocomposite exhibits a significantly lower PL intensity peak than CdO/ZnS. After illumination for 80 min, ZnS, CdO, and CdO/ZnS showed the lower photocatalytic performance with degradation efficiencies of 20.27%, 35.13% and 68.41%, respectively. Furthermore, the Fe<sup>3+</sup>-doped CdO/ZnS nanocomposite exhibited the strongest photocatalytic activity and arrived at the optimum photocatalytic degradation activity (97.06%) after 80 min. The kinetic rate constant of the Fe<sup>3+</sup>-doped CdO/ZnS nanocomposite was found to be 0.0341 min<sup>-1</sup>, and it is about 11.37, 5.98, and 2.41 times over ZnS, CdO and CdO/ZnS, respectively. The radical trapping experiments have proved that •OH radicals are the main active species generated in the photocatalytic reaction. Therefore, the superior photocatalytic activity is attributed to the formation of interfacial contact and defect energy levels of the doped ions, which can greatly extend the lifetime of the electron–hole pair but also enhance the light absorption.

**Supplementary Materials:** The following supporting information can be downloaded at: <https://www.mdpi.com/article/10.3390/catal13091312/s1>, Figure S1: Compositional analysis of the Fe<sup>3+</sup>-doped CdO/ZnS nanocomposite; Figure S2: SEM images of Fe<sup>3+</sup>-doped CdO/ZnS nanocomposite (a) before and (b) after stability test; Figure S3: TEM images of Fe<sup>3+</sup>-doped CdO/ZnS nanocomposite (a) before and (b) after stability test.

**Author Contributions:** Conceptualization, methodology and writing—original draft preparation: R.J.S.; Methodology and writing—original draft preparation: I.S.; Conceptualization, methodology and writing—original draft preparation: T.R.G.; Conceptualization, supervision and review: R.V.S.S.N.R.; Conceptualization, supervision, formal analysis and review: R.K. All authors have read and agreed to the published version of the manuscript.

**Funding:** This research received no external funding.

**Data Availability Statement:** Data available on request from the corresponding authors.

**Conflicts of Interest:** The authors have no conflict of interest to declare that are relevant to the content of this article.

## References

1. Lotfi, S.; Ouardi, M.E.; Ahsaine, H.A.; Assani, A. Recent progress on the synthesis, morphology and photocatalytic dye degradation of BiVO<sub>4</sub> photocatalysts: A review. *Catal. Rev.* **2022**, 1–45. [[CrossRef](#)]
2. Kumari, H.; Sonia; Suman; Ranga, R.; Chahal, S.; Devi, S.; Sharma, S.; Kumar, S.; Kumar, P.; Kumar, S.; et al. A Review on Photocatalysis Used for Wastewater Treatment: Dye Degradation. *Water Air Soil Pollut.* **2023**, *234*, 349. [[CrossRef](#)] [[PubMed](#)]
3. Luo, Y.; Zheng, A.; Li, J.; Han, Y.; Xue, M.; Zhang, L.; Yin, Z.; Xie, C.; Chen, Z.; Ji, L.; et al. Integrated adsorption and photodegradation of tetracycline by bismuth oxycarbonate/biochar nanocomposites. *Chem. Eng. J.* **2023**, *457*, 141228. [[CrossRef](#)]
4. Murugadoss, G.; Muruganandam, S.; Kumar, M.R.; Pugazhendhi, A. Ultrafast photodegradation of textile industry dyes using efficient sulfide based ternary nanocomposites. *Chemosphere* **2023**, *336*, 139100. [[CrossRef](#)]
5. Rabeie, B.; Mahmoodi, N.M. Hierarchical ternary titanium dioxide decorated with graphene quantum dot/ZIF-8 nanocomposite for the photocatalytic degradation of doxycycline and dye using visible light. *J. Water Process Eng.* **2023**, *54*, 103976. [[CrossRef](#)]
6. Ur Rahman, Z.; Shah, U.; Alam, A.; Shah, Z.; Shaheen, K.; Bahadar Khan, S.; Ali Khan, S. Photocatalytic degradation of cefixime using CuO-NiO nanocomposite photocatalyst. *Inorg. Chem. Commun.* **2023**, *148*, 110312. [[CrossRef](#)]
7. Pramanick, B.; Chawla, M.; Siril, P.F. Photocatalytic degradation of aromatic pollutants using plasmonic Cu-Ag nanocomposites. *Opt. Mater.* **2023**, *137*, 113553. [[CrossRef](#)]
8. Shah, A.H.; Rather, M.A. Ultrasonically assisted hydrothermal synthesis of tungsten(VI) oxide-TiO<sub>2</sub> nanocomposites for enhanced photocatalytic degradation of non-narcotic drug paracetamol under natural solar light: Insights into degradation pathway, mechanism, and toxicity assessment. *Environ. Sci. Pollut. Res.* **2023**, *30*, 93916–93933. [[CrossRef](#)]
9. Aruljothi, C.; Balaji, P.; Vaishnavi, E.; Pazhanivel, T.; Vasuki, T. Magnetic recyclable CuFe<sub>2</sub>O<sub>4</sub>/rGO nanocomposite for the degradation of tetracycline under sunlight irradiation. *J. Chem. Technol. Biotechnol.* **2023**, *98*, 1908–1917. [[CrossRef](#)]
10. Sreeram, N.; Aruna, V.; Koutavarapu, R.; Lee, D.-Y.; Rao, M.C.; Shim, J. Fabrication of InVO<sub>4</sub>/SnWO<sub>4</sub> heterostructured photocatalyst for efficient photocatalytic degradation of tetracycline under visible light. *Environ. Res.* **2023**, *220*, 115191. [[CrossRef](#)]
11. El Messaoudi, N.; Ciğeroğlu, Z.; Şenol, Z.M.; Elhajam, M.; Noureen, L. A comparative review of the adsorption and photocatalytic degradation of tetracycline in aquatic environment by g-C<sub>3</sub>N<sub>4</sub>-based materials. *J. Water Process Eng.* **2023**, *55*, 104150. [[CrossRef](#)]
12. Cao, M.; Xu, P.; Tian, K.; Shi, F.; Zheng, Q.; Ma, D.; Zhang, G. Recent advances in microwave-enhanced advanced oxidation processes (MAOPs) for environmental remediation: A review. *Chem. Eng. J.* **2023**, *471*, 144208. [[CrossRef](#)]
13. Taoufik, N.; Sadiq, M.h.; Abdennouri, M.; Qourzal, S.; Khataee, A.; Sillanpää, M.; Barka, N. Recent advances in the synthesis and environmental catalytic applications of layered double hydroxides-based materials for degradation of emerging pollutants through advanced oxidation processes. *Mater. Res. Bull.* **2022**, *154*, 111924. [[CrossRef](#)]
14. Mahmoudi, F.; Saravanakumar, K.; Maheskumar, V.; Njaramba, L.K.; Yoon, Y.; Park, C.M. Application of perovskite oxides and their composites for degrading organic pollutants from wastewater using advanced oxidation processes: Review of the recent progress. *J. Hazard. Mater.* **2022**, *436*, 129074. [[CrossRef](#)]
15. Singh, A.K.; Gautam, R.K.; Agrahari, S.; Prajapati, J.; Tiwari, I. Graphene oxide supported Fe<sub>3</sub>O<sub>4</sub>-MnO<sub>2</sub> nanocomposites for adsorption and photocatalytic degradation of dyestuff: Ultrasound effect, surfactants role and real sample analysis. *Int. J. Environ. Anal. Chem.* **2022**, 1–27. [[CrossRef](#)]
16. elbakry, S.; Ali, M.E.A.; Abouelfadl, M.; Badway, N.A.; Salam, K.M.M. Effective removal of organic compounds using a novel cellulose acetate coated by PA/g-CN/Ag nanocomposite membranes. *Surf. Interfaces* **2022**, *29*, 101748. [[CrossRef](#)]
17. Gubitosa, J.; Mongiovi, C.; Romita, R.; Cosma, P.; Nuzzo, S.; Rizzi, V.; Fini, P. Removal of Emerging Contaminants from Water Using Cyclodextrin-Based Polymers and Advanced Oxidation Processes: The Case of Carbamazepine. *Processes* **2022**, *10*, 1703. [[CrossRef](#)]

18. Peramune, D.; Manatunga, D.C.; Dassanayake, R.S.; Premalal, V.; Liyanage, R.N.; Gunathilake, C.; Abidi, N. Recent advances in biopolymer-based advanced oxidation processes for dye removal applications: A review. *Environ. Res.* **2022**, *215*, 114242. [[CrossRef](#)]
19. Massoud, A.; El-Mehasseb, I.; Saad Allah, M.; Elmahallawy, E.K.; Alsharif, K.F.; Ahmed, M.S.; Derbalah, A.S. Advanced Oxidation Processes Using Zinc Oxide Nanocatalyst for Detoxification of Some Highly Toxic Insecticides in an Aquatic System Combined with Improving Water Quality Parameters. *Front. Environ. Sci.* **2022**, *10*, 227. [[CrossRef](#)]
20. Kusmirek, E. A CeO<sub>2</sub> Semiconductor as a Photocatalytic and Photoelectrocatalytic Material for the Remediation of Pollutants in Industrial Wastewater: A Review. *Catalysts* **2020**, *10*, 1435. [[CrossRef](#)]
21. Belousov, A.S.; Parkhacheva, A.A.; Suleimanov, E.V.; Fukina, D.G.; Koryagin, A.V.; Shafiq, I.; Krasheninnikova, O.V.; Kuzmichev, V.V. Doping vs. heterojunction: A comparative study of the approaches for improving the photocatalytic activity of flower-like Bi<sub>2</sub>WO<sub>6</sub> for water treatment with domestic LED light. *Catal. Commun.* **2023**, *180*, 106705. [[CrossRef](#)]
22. Humayun, M.; Raziq, F.; Khan, A.; Luo, W. Modification strategies of TiO<sub>2</sub> for potential applications in photocatalysis: A critical review. *Green Chem. Lett. Rev.* **2018**, *11*, 86–102. [[CrossRef](#)]
23. Ahmadi, A.; Hajilou, M.; Zavari, S.; Yaghmaei, S. A comparative review on adsorption and photocatalytic degradation of classified dyes with metal/non-metal-based modification of graphitic carbon nitride nanocomposites: Synthesis, mechanism, and affecting parameters. *J. Clean. Prod.* **2023**, *382*, 134967. [[CrossRef](#)]
24. Kumar, S.; Kaushik, R.D.; Purohit, L.P. Novel ZnO tetrapod-reduced graphene oxide nanocomposites for enhanced photocatalytic degradation of phenolic compounds and MB dye. *J. Mol. Liq.* **2021**, *327*, 114814. [[CrossRef](#)]
25. Lwin, H.M.; Zhan, W.; Song, S.; Jia, F.; Zhou, J. Visible-light photocatalytic degradation pathway of tetracycline hydrochloride with cubic structured ZnO/SnO<sub>2</sub> heterojunction nanocatalyst. *Chem. Phys. Lett.* **2019**, *736*, 136806. [[CrossRef](#)]
26. Upadhyay, G.K.; Rajput, J.K.; Pathak, T.K.; Pal, P.K.; Purohit, L.P. Tailoring and optimization of hybrid ZnO:TiO<sub>2</sub>:CdO nanomaterials for advance oxidation process under visible light. *Appl. Surf. Sci.* **2020**, *509*, 145326. [[CrossRef](#)]
27. Kumar, S.; Kaushik, R.D.; Purohit, L.P. ZnO-CdO nanocomposites incorporated with graphene oxide nanosheets for efficient photocatalytic degradation of bisphenol A, thymol blue and ciprofloxacin. *J. Hazard. Mater.* **2022**, *424*, 127332. [[CrossRef](#)]
28. Jayasankari, S.; Pramothkumar, A.; Mani, P. Facile synthesis and characterization of ZnO NPs, ZnO/CdO and ZnO/SnO<sub>2</sub> nanocomposites for photocatalytic degradation of Eosin Yellow and Direct Blue 15 under UV light irradiation. *J. Mater. Sci. Mater. Electron.* **2022**, *33*, 9858–9874. [[CrossRef](#)]
29. Upadhyay, G.K.; Rajput, J.K.; Pathak, T.K.; Swart, H.C.; Purohit, L.P. Photoactive CdO:TiO<sub>2</sub> nanocomposites for dyes degradation under visible light. *Mater. Chem. Phys.* **2020**, *253*, 123191. [[CrossRef](#)]
30. Gusain, R.; Kumar, N.; Opoku, F.; Govender, P.P.; Ray, S.S. MoS<sub>2</sub> Nanosheet/ZnS Composites for the Visible-Light-Assisted Photocatalytic Degradation of Oxytetracycline. *ACS Appl. Nano Mater.* **2021**, *4*, 4721–4734. [[CrossRef](#)]
31. Okla, M.K.; Janani, B.; Swetha, S.; Alatar, A.A.; Alaraidh, I.A.; Al-ghamdi, A.A.; Abdelaziz, R.F.; Abdel-Maksoud, M.A.; Rahiman, M.K.; Khan, S.S. Environmental friendly nano-star CdS coupled ZnS on bi-polymer matrix: Unravelling defects-rich nanoplatform for ultrahigh white light active direct S-scheme photodegradation of organic pollutants. *J. Alloys Compd.* **2022**, *925*, 166611. [[CrossRef](#)]
32. Meena, P.L.; Poswal, K.; Surela, A.K.; Saini, J.K. Facile synthesis of ZnO/CuO/Ag<sub>2</sub>O ternary metal oxide nanocomposite for effective photodegradation of organic water pollutants. *Water Sci. Technol.* **2021**, *84*, 2615–2634. [[CrossRef](#)] [[PubMed](#)]
33. Koli, P.B.; Kapadnis, K.H.; Deshpande, U.G. Transition metal decorated Ferrosferric oxide (Fe<sub>3</sub>O<sub>4</sub>): An expeditious catalyst for photodegradation of Carbol Fuchsin in environmental remediation. *J. Environ. Chem. Eng.* **2019**, *7*, 103373. [[CrossRef](#)]
34. Rajput, J.K.; Pathak, T.K.; Kumar, V.; Swart, H.C.; Purohit, L.P. Controlled sol-gel synthesis of oxygen sensing CdO:ZnO hexagonal particles for different annealing temperatures. *RSC Adv.* **2019**, *9*, 31316–31324. [[CrossRef](#)]
35. Li, H.; Wang, J.; Zhao, Y.; Tan, T. Synthesis of the ZnO@ZnS Nanorod for Lithium-Ion Batteries. *Energies* **2018**, *11*, 2117. [[CrossRef](#)]
36. Rajesh Kumar, B.; Hymavathi, B. X-ray peak profile analysis of Sb<sub>2</sub>O<sub>3</sub>-doped ZnO nanocomposite semiconductor. *Adv. Nat. Sci. Nanosci. Nanotechnol.* **2018**, *9*, 035018. [[CrossRef](#)]
37. Abebe, B.; Tsegaye, D.; Sori, C.; Renuka Prasad, R.C.k.; Murthy, H.C.A. Cu/CuO-Doped ZnO Nanocomposites via Solution Combustion Synthesis for Catalytic 4-Nitrophenol Reduction. *ACS Omega* **2023**, *8*, 9597–9606. [[CrossRef](#)]
38. Kim, K.-Y.; Kwak, J.-S.; An, Y.-I.; Oh, K.-R.; Kwon, Y.-U. Characteristics of NaNO<sub>3</sub>-Promoted CdO as a Midtemperature CO<sub>2</sub> Absorbent. *ACS Appl. Mater. Interfaces* **2017**, *9*, 21563–21572. [[CrossRef](#)]
39. Nguyen, Q.H.; Park, T.; Hur, J. Enhanced Cycle Stability of Zinc Sulfide Anode for High-Performance Lithium-Ion Storage: Effect of Conductive Hybrid Matrix on Active ZnS. *Nanomaterials* **2019**, *9*, 1221. [[CrossRef](#)]
40. Feng, D.-M.; Sun, Y.; Yuan, Z.-Y.; Fu, Y.; Jia, B.; Li, H.; Ma, T. Ampoule method fabricated sulfur vacancy-rich N-doped ZnS electrodes for ammonia production in alkaline media. *Mater. Renew. Sustain. Energy* **2021**, *10*, 8. [[CrossRef](#)]
41. Jeejamol, D.J.; Raj, A.M.E.; Jayakumari, K.; Ravidhas, C. Optimization of CdO nanoparticles by Zr<sup>4+</sup> doping for better photocatalytic activity. *J. Mater. Sci. Mater. Electron.* **2018**, *29*, 97–116. [[CrossRef](#)]
42. Jeejamol, D.J.; Raj, A.M.E.; Aultrin, K.S.J. Alteration of CdO Lattice Structure By Cu<sup>2+</sup> Doping for Enhanced Photocatalytic Application. *Braz. J. Phys.* **2021**, *51*, 1550–1564. [[CrossRef](#)]
43. Kumar, P.; Mathpal, M.C.; Inwati, G.K.; Kumar, S.; Duvenhage, M.-M.; Roos, W.D.; Swart, H.C. Study of Defect-Induced Chemical Modifications in Spinel Zinc-Ferrites Nanostructures by In-Depth XPS Investigation. *Magnetochemistry* **2023**, *9*, 20. [[CrossRef](#)]

44. Dai, L.; Strelow, C.; Kipp, T.; Mews, A.; Benkenstein, I.; Eifler, D.; Vuong, T.H.; Rabeah, J.; McGettrick, J.; Lesyuk, R.; et al. Colloidal Manganese-Doped ZnS Nanoplatelets and Their Optical Properties. *Chem. Mater.* **2021**, *33*, 275–284. [[CrossRef](#)]
45. Tamtam, M.R.; Koutavarapu, R.; Shim, J. InVO<sub>4</sub> nanosheets decorated with ZnWO<sub>4</sub> nanorods: A novel composite and its enhanced photocatalytic performance under solar light. *Environ. Res.* **2023**, *227*, 115735. [[CrossRef](#)] [[PubMed](#)]
46. Wang, C.; Ran, W.; Du, P.; Li, W.; Luo, L.; Wang, D. Enhanced Visible Light-Driven Photocatalytic Activities and Photoluminescence Characteristics of BiOF Nanoparticles Determined via Doping Engineering. *Inorg. Chem.* **2020**, *59*, 11801–11813. [[CrossRef](#)] [[PubMed](#)]
47. Nishanth, S.; Nivithaa, S.; Sridhar, C.; Nagaraja, K.S.; Karnan, C. Structural, spectral and photoluminescence analyses of Fe<sup>3+</sup> doped methyl hydroxy(diphenyl)ethanoate (MHE) crystal. *J. Mol. Struct.* **2023**, *1285*, 135501. [[CrossRef](#)]
48. Koutavarapu, R.; Peera, S.G.; Lee, T.G.; Myla, C.R.; Lee, D.-Y.; Shim, J.; Balasingam, S.K. Recent Trends in Graphitic Carbon Nitride-Based Binary and Ternary Heterostructured Electrodes for Photoelectrochemical Water Splitting. *Processes* **2021**, *9*, 1959. [[CrossRef](#)]
49. Govinda, D.; Prabhakara, S.R.M.; Dakshina Murthy, P. Enhanced photocatalytic activity in hydro-thermally grown nano structured ZnO/SnS core-shell composites. *Z. Naturforsch.* **2021**, *77*, 153–169.
50. Karthik, K.; Radhika, D.; Nikolova, M.P.; Andal, V.; Kishor Kumar, S.; Sivarama Krishna, L. Facile microwave-assisted synthesis of metal oxide CdO-CuO nanocomposite: Photocatalytic and antimicrobial enhancing properties. *Optik* **2020**, *218*, 165112.
51. Gurugubelli, T.R.; Ravikumar, R.V.S.S.N.; Koutavarapu, R. Enhanced Photocatalytic Activity of ZnO-CdS Composite Nanostructures towards the Degradation of Rhodamine B under Solar Light. *Catalysts* **2022**, *12*, 84. [[CrossRef](#)]
52. Zgura, I.; Preda, N.; Socol, G.; Ghica, C.; Ghica, D.; Enculescu, M.; Negut, I.; Nedelcu, L.; Frunza, L.; Ganea, C.P.; et al. Wet chemical synthesis of ZnO-CdS composites and their photocatalytic activity. *Mat. Res. Bull.* **2018**, *99*, 174–181. [[CrossRef](#)]
53. Rao, G.T.; Ravikumar, R.V.S.S.N. Novel Fe-doped ZnO-CdS nanocomposite with enhanced visible light-driven photocatalytic performance. *Mat. Res. Innov.* **2021**, *25*, 215–220. [[CrossRef](#)]
54. Govinda, D.; Thirumala Rao, G.; Prabhakara, S.R.M.; Bathula, B.; Kisoo, Y. Facile Synthesis, Characterization, and Photocatalytic Activity of Hydrothermally Grown Cu<sup>2+</sup>-Doped ZnO-SnS Nanocomposites for MB Dye Degradation. *Catalysts* **2022**, *12*, 328.
55. Govinda, D.; Thirumala Rao, G.; Viswanadham, B.; Bathula, B.; Kisoo, Y. Novel In Situ Fabrication of Fe-Doped Zinc Oxide/Tin Sulfide Heterostructures for Visible-Light-Driven Photocatalytic Degradation of Methylene Blue. *J. Chem.* **2023**, *1407395*, 13.
56. Salunkhe, T.T.; Govinda, D.; Gurugubelli, T.R.; Bathula, B.; Kisoo, Y. Direct Hydrothermally Synthesized Novel Z-Scheme Dy<sup>3+</sup>-Doped ZnO/SnS Nanocomposite for Rapid Photocatalytic Degradation of Organic Contaminants. *Catalysts* **2023**, *13*, 1292. [[CrossRef](#)]
57. Govinda, D.; Srinivasa Rao, M.P.; Potukuchi, D.M. Visible light driven robust photocatalytic activity in vanadium-doped ZnO/SnS core-shell nanocomposites for decolorization of MB dye towards wastewater treatment. *Inorg. Nano Metal Chem.* **2022**, *52*, 1059–1076.
58. Reza Delsouz Khaki, M.; Saleh Shafeeyan, M.; Abdul Aziz, A.R.; Wan Mohd Ashri, W.D. Evaluating the efficiency of nano-sized Cu doped TiO<sub>2</sub>/ZnO photocatalyst under visible light irradiation. *J. Mol. Liq.* **2018**, *258*, 354–365. [[CrossRef](#)]

**Disclaimer/Publisher's Note:** The statements, opinions and data contained in all publications are solely those of the individual author(s) and contributor(s) and not of MDPI and/or the editor(s). MDPI and/or the editor(s) disclaim responsibility for any injury to people or property resulting from any ideas, methods, instructions or products referred to in the content.